Lawrence Berkeley National Laboratory

LBL Publications

Title

X-ray radiolytic labeling reveals the molecular basis of orange carotenoid protein photoprotection and its interactions with fluorescence recovery protein

Permalink

https://escholarship.org/uc/item/9sh115mq

Journal

Journal of Biological Chemistry, 294(22)

ISSN

0021-9258

Authors

Gupta, Sayan

Sutter, Markus

Remesh, Soumya G

et al.

Publication Date

2019-05-01

DOI

10.1074/jbc.ra119.007592

Peer reviewed

eScholarship.org Powered by the California Digital Library
University of California

X-ray radiolytic labeling reveals the molecular basis of orange carotenoid protein photoprotection and its interactions with fluorescence recovery protein

Sayan Gupta[1], Markus Sutter[1,2,3], Soumya G. Remesh[1], Maria Agustina Dominguez-Martin[2], Han Bao[2], Xinyu A. Feng[1], Leanne-Jade G. Chan[4], Christopher J. Petzold[4], Cheryl A. Kerfeld[1, 2, 3]* and Corie Y. Ralston[1]*

[1] Molecular Biophysics and Integrated Bioimaging Division, Lawrence Berkeley National Laboratory, Berkeley, CA 94720; [2] MSU-DOE Plant Research Laboratory and Department of Biochemistry and Molecular Biology, Michigan State University, East Lansing, MI 48824; [3]Environmental Genomics and Systems Biology Division, Lawrence Berkeley National Laboratory, Berkeley, CA 94720; [4] Biological Systems and Engineering Divisions, Lawrence Berkeley National Laboratory, Berkeley, CA 94720

Running title: *X-ray footprinting reveals OCP photoprotection*

* To whom correspondence should be addressed:
Corie Y. Ralston, Molecular Biophysics and Integrated Bioimaging Division, Lawrence Berkeley National Laboratory, Berkeley, California 94720; cyralston@lbl.gov, Tel. (510) 495-2594.
and
Cheryl A. Kerfeld, MSU-DOE Plant Research Laboratory, Michigan State University, East Lansing, Michigan 48824; ckerfeld@lbl.gov, Tel. (517) 432-4371.

Keywords: Orange Carotenoid Protein (OCP), carotenoid chromophore, time-resolved X-ray footprinting, Fluorescence Recovery Protein (FRP), non-photochemical quenching (NPQ), antenna complex, phycobilisome, photosynthesis, photoprotection, X-ray footprinting with mass spectrometry (XFMS)

Abstract

In cyanobacterial photoprotection, the orange carotenoid protein (OCP) is photoactivated under excess light conditions and binds to the light-harvesting antenna, triggering the dissipation of captured light energy. In low light, the OCP relaxes to the native state, a process that is accelerated in the presence of fluorescence recovery protein (FRP). Despite the importance of the OCP in photoprotection, the precise mechanism of photoactivation by this protein is not well understood. Using time-resolved X-ray-mediated *in situ* hydroxyl radical labeling, we probed real-time solvent accessibility (SA) changes at key OCP residues during photoactivation and relaxation. We observed a biphasic photoactivation process in which carotenoid migration preceded domain dissociation. We also observed a multiphasic relaxation process, with collapsed domain association preceding the final conformational rearrangement of the carotenoid. Using steady-state hydroxyl-radical labeling, we identified sites of interaction between the FRP and OCP. In combination, the findings in this study provide molecular-level insights into the factors driving structural changes during OCP-mediated photoprotection in cyanobacteria, and furnish a basis for understanding the physiological relevance of the FRP- mediated relaxation process.

Introduction

Photosynthetic organisms have a protective mechanism known as nonphotochemical quenching (NPQ) to dissipate excess energy and prevent oxidative damage, which would otherwise lead to cell death under high light conditions (1). Unlike plants and algae, in which the NPQ mechanism involves membrane-embedded protein-pigment

interactions within light-harvesting complexes, cyanobacteria use the orange carotenoid protein (OCP) to trigger photoprotection of their extramembrane, water-soluble antenna complexes called the phycobilisomes (PB) (2). Upon absorption of blue-green light, dark-adapted OCP (OCP^O) switches to the active, red form (OCP^R), which interacts with the PB and effectively reduces the amount of energy transferred to the photochemical reaction center. The OCP^R form is metastable; it relaxes back to OCP^O slowly in darkness, but instantaneously in the presence of the fluorescence recovery protein (FRP) (3-5). The FRP plays an important role in the photoprotective mechanism by detaching the OCP^R from PB and accelerating the OCP^R to OCP^O conversion to restore ambient photosynthesis. Determining the exact structural changes that accompany OCP^R formation and its interactions with the FRP is critical for a complete mechanistic understanding of the regulation of NPQ in cyanobacteria. OCP^O, which crystallizes as an antiparallel dimer, is composed of an all-helical N-terminal domain (NTD), and a mixed α/β C-terminal domain (CTD) (6,7). A noncovalently bound carotenoid spans both domains in the OCP^O. The NTD and CTD interact through two regions, the major interface, which buries 1722 $Å^2$ of surface area, and the minor interface, which is the interaction region between the N-terminal alpha helix (αA) and the CTD (6,7). The FRP, in contrast, is 13 kDa and entirely α-helical. The FRP has been captured in two distinct conformations, with distinct quarternary structures, in a single crystal form (5). The first high-resolution structural information on full-length monomeric OCP^R in solution was obtained by the combination of structural methods of X-ray crystallography, X-ray radiolytic labeling or X-ray Footprinting with mass spectrometry (XFMS), hydrogen/deuterium exchange with mass spectrometry (HDX-MS), and small angle scattering (SAXS) (8). These results showed that upon photoactivation the chromophore translocates 12 Å into the NTD, and the NTD and CTD completely dissociate from each other. In order to understand how chromophore movement might be linked to larger conformational changes in the protein, XFMS was further used to pinpoint subtle structural changes in the specific amino acids and structurally conserved water molecules along a potential signal propagation pathway from carotenoid to the protein surface (8). Recently, crystallography has captured light induced initial structural changes in the dimeric form of the OCP (9). Collectively, these data provided a comprehensive view of global and local intra-protein structural endpoints at the start and end of photoactivation, but could not delineate the steps along the temporal path during OCP photoactivation and how FRP accelerates the relaxation process.

UV-visible absorption, which is an important analytical tool to characterize OCP^O and OCP^R, is highly sensitive to the interactions of multiple amino acid side chains with the carotenoid and to the polarity of the carotenoid binding pocket (7,10). The time course of UV-visible absorption, which occurs in minutes at room temperature, represents the overall kinetics resulting from the change in the carotenoid-protein interaction and/or environment, but cannot delineate specific changes that result/occur in the protein domain and distant from the carotenoid binding site (7). Although carotenoid dynamics during photoactivation in the OCP has been studied by ultrafast spectroscopic methods (11-13), which have revealed details of the electronic structure of short-lived carotenoid excited states and suggested changes in the conformational orientation of the carotenoid, these studies have not provided any direct information on the global structural changes in the protein occurring on a longer timescale during photoactivation or relaxation. Intrinsic fluorescence from tryptophan and other aromatic amino acids also provides an overall picture of the dynamics of photoactivation in seconds but represents an ensemble average of protein conformation resulting from multiple aromatic residues (12,14). Binding assays using size exclusion chromatography together with mutational analysis have indicated that the minor interface and the CTD influence the OCP-FRP interaction and have revealed the variable stoichiometry of the FRP-OCP complex (14,15). These data provide a global

view of OCP-FRP interactions and indicate likely surface regions involved in the interactions, but do not pinpoint the specific residue interactions necessary to provide a mechanistic understanding of the recovery of OCP^R by FRP for the regulation of NPQ.

XFMS is ideally suited for revealing conformational dynamics at the single residue level. In this method, a high flux density X-ray beam ionizes water to produce hydroxyl radicals *in situ* and covalently modifies amino acid side chains on the microsecond timescale (16,17). These modifications are analyzed by high-resolution mass spectrometry to locate the sites and extent of modification. Here, we used time-resolved XFMS to study the OCP photocycle in solution in real time. We captured the progress of OCP^R formation from OCP^O under constant blue light illumination, and also the reverse process of OCP^R relaxation to OCP^O under dark conditions by exposing the sample to X-rays at time intervals of seconds to minutes. The residue-specific and time-dependent solvent accessibility (SA) changes provide a mechanistic understanding of the carotenoid induced signal transfer within the protein under native conditions. Further, we monitored the residue-specific SA changes in the formation of complexes of OCP-FRP and CTD-FRP. We identified a binding site on the CTD domain of the OCP and, in addition, the data indicate that the FRP interacts with the OCP at a second location on the N-terminal alpha helix. These data support a previous suggestion that the FRP effectively holds together the OCP domains at the major and minor interfaces, and that this forced proximity of the two domains is what leads to the acceleration of OCP^R relaxation to OCP^O (14). Furthermore, by temporally differentiating SA changes we have identified residue-level events that at least partially constitute the driving force for the global conformational changes that underlie activation and relaxation, and have pinpointed the exact sequence of these structural changes.

Results

Time-evolution of residue-specific conformation changes in OCP photoactivation and relaxation

To follow the activation of OCP^O to OCP^R , we continuously illuminated OCP^O with blue light, and after selected delays, subjected the protein to a 200-microsecond pulse of synchrotron X-rays (17) (Fig. 1a). The microsecond X-ray pulse ionizes both bulk and bound water rapidly and isotropically to generate hydroxyl radicals *in-situ*, which then react with proximal residues to yield stable modification products (18). As photoactivation progresses, XFMS captures sequential snapshots of changing SAs of the various residues in parallel across the protein. Following X-ray exposure, samples were digested and then analyzed by high-pressure liquid chromatography and mass spectrometry (LC-MS), which generated > 94% sequence coverage and identified all the side-chain modifications reported in our previous studies (8). To follow the relaxation process, pre-illuminated OCP^R in the dark was subjected to microsecond pulses after various selected delay times (Fig. 2a). For both experiments, the sample conditions were chosen so as to enable comparison with previous steady-state XFMS and complement UV-visible studies at 15° C (Fig. 1b) (8,10). The plot of the fraction of unmodified side chain vs. delay time produced residue-specific kinetics traces which show that photoactivation and relaxation followed a different pathway (Fig 1c and Fig 2a). The time-resolved XFMS strategy thus provided both a qualitative view and quantitative measure of the lifetime of local conformational changes at a high structural resolution and was able to follow these changes at various residues as a function of time during photoactivation or relaxation.

The OCP^O photoactivation pathway is concerted

The site-specific kinetic progress curves obtained for the OCP^O to OCP^R photoactivation process showed a single component or was biphasic in all cases (Fig. 1c and Fig. S1), and the overall trend of SA changes were consistent with our previous steady state XFMS experiments (8). Although

the time-dependent progress curve consists of a single component, the result can be interpreted by three general categories of conformational transition (Fig 1d, and Table S1): In the first category, residues Trp41, Tyr44 and Met47, which are located in the carotenoid binding pocket of the NTD, displayed SA changes on the fastest timescale (τ = < 1.5 min). The overall decrease in SA during photoactivation is consistent with the movement of the carotenoid deeper into the binding pocket in the NTD, as observed previously (8), and indicates that rearrangement within the carotenoid tunnel is one of the first structural changes after chromophore activation by light (8,9). In the second category (1.5 min < τ < 3.5 min) were residues at the major interface (Tyr98, Trp101, Pro103, Arg155, Asn156, Pro276, Trp277, Phe278, and Met284) and NTD residues Phe163, Lys167, residues 172-185, and Phe227. Most of these residues are at the major interface, suggesting that domain dissociation is completed after the movement of the carotenoid. In the third or slowest category (τ > 3.5 min) were the NTD αA (Ala8, Arg9) and its adjacent helical region (13-22), residues at the minor interface which are in proximity to the CTD residues 255-268, 298-299, 301-303 and the loop joining the NTD (residues 119-146). Together, this data suggests that the sequence of events begin with carotenoid migration, followed by domain separation at the major interface, and subsequent detachment of the NTD αA at the minor interface. We emphasize here that the relative order of events in photoactivation is significant, rather than the specific lifetime of each step, as these will be affected by experimental conditions such as light intensity or ionic strength of the buffer. In particular, the light intensity is of critical importance because of spontaneous reversal of OCP^O to OCP^R.

OCP relaxation occurs through a compact intermediate

The OCP^R to OCP^O relaxation follows a single exponential decay with a lifetime of ~ 10 min when measured by the absorbance change at 550 nm at 15 °C (Fig. 1a) (12). In contrast, XFMS kinetic progress curves did not show a smooth transition from initial to end state, but instead a complex curve consisting of an initial component representing a change to a more compact (less accessible) state, followed by a slower transition to a more accessible state, and then a final transition to the end state, which could be either more or less accessible than the initial state depending on the specific residue (Fig. 2a and Fig. S2). While the relative amplitude of SA changes within the kinetic progress curves varied, all of them showed three main components (Fig 2b, and Table S2). The first component entailed a decrease in SA with a lifetime of 0.5 - 2 min. An increase in SA followed this step with a lifetime of 2 – 3 min, and then a slow decrease in SA with a lifetime of 5 - 10 min. In all cases, the net SA changes we observed in the relaxation process corroborate our steady-state data on the relaxation process, which involves re-association of the minor and major interface, movement of the carotenoid to span both domains, and attachment of the NTD αA (8). The time constraints to conduct XFMS at the beamline facility and subsequent mass spectrometry measurements generated a limited number of data points in the time-resolved progress curves in contrast to other contemporary spectroscopic approaches. However, the trend of SA changes was reproducible, and the simulated multiexponential trace provides a clear temporal view of these residue-specific changes. To simplify our interpretation, we categorized site-specific kinetic progress curves into two, fast and slow, based on the relative amplitude of SA changes of the kinetic components (Table S2). Within the slow category, we identified two sub-categories representing curves for which there is a net accessibility change from initial to final state and curves for which there is no net accessibility change.

The fast category consisted of progress curves in which the first component showed an initial large decrease in SA within 0.5-2 min, and after that only small reciprocal changes, implying that most of the structural rearrangement for these residues in the relaxation process were completed early on,

followed by minor conformational readjustments leading to OCP^O. Residues in this category -- Ala8, Arg9, residues 13-22, Tyr98, Trp101, Pro103, Arg155, Asn156, Pro259, Phe264, Lys268, Pro276, Trp277, Phe278, Met284, Phe290, Ile298, Phe299, Val301, Ala302, and Ile303 -- are located at the major and minor interfaces. Most of these residues are involved in an inter-domain H-bonding network between conserved water clusters and directly involved in the signal transfer from carotenoid to the surface of the protein (8). The second category is comprised of progress curves which showed a considerable change in SA in the second component, and which occurred on a timescale of 10 minutes. We further subdivided these curves into two subcategories. The NTD residues Pro2, Phe3, Trp41, Tyr44, Met47, Phe121, Pro124, Pro126, Phe163, Pro175, Pro178, Pro179, Arg185, and CTD residues Pro225, Phe227, and Pro230 were in the first subcategory. These residues showed an overall increase in accessibility and are consistent with structural determinants retrieved from our previous steady state XFMS studies (8). Residues Trp41, Tyr44, and Met47 are important for carotenoid translocation and stabilization, residues P175 to R185 are on the linker joining the NTD and CTD, and residues Pro225 to Pro230 are involved in stabilization of the inter-domain H-bonding network. The decrease in SA in the first phase indicated exclusion of local water from critical regions of OCP^R and formation of a compact intermediate state, which is unlike that of the native OCP^O. We observed that the reciprocal ratio of net SA change between the first and the second kinetic components was approximately 1:2 (Table S2). Therefore, the second component resulted in major rearrangements in the water-sidechain H-bonding network in the chromophore binding pocket to establish the native-like state of OCP^O. The presence of the slow decrease in SA in the third component might be due to further conformational rearrangements for the formation of final dark-adapted OCP^O. The NTD residues Met74, Met83, Pro94, Phe109, Trp110, Tyr111, Met117, Met161, Lys167, and CTD residues Met202, Leu291-292, Pro297, Pro309, Lys310 fell into the second subcategory. For these residues, the SA decreased and then increased in a 1:1 ratio (Table S2), resulting in no net SA change. This observation is consistent with previous studies (8) in which many of these residues showed no net change in SA upon photoactivation, but here, the decrease in SA or compaction in the first component of the kinetic trace might indicate an incorrectly folded intermediate in the relaxation process. The relaxation process is temperature dependent and is slowed significantly at lower temperatures. To confirm the formation of a compact kinetic intermediate we carried out the same experiment at 4°C, collecting accessibility changes from 0 to 30 min in the OCP^R to OCP^O transition (Fig 2a lower panel and Fig. S3). The progressive decrease in SA of all residues further supports the formation of a compact intermediate state in the OCP^R to OCP^O relaxation process.

XFMS reveals contacts between the OCP and the FRP by the comparative SA analysis between the OCP and OCP/CTD-FRP complexes

To determine the interaction between of the FRP and OCP, we conducted steady-state XFMS analysis on the OCP and its complex with FRP. We subjected isolated CTD, OCP^O, OCP^R and their respective complexes with FRP to a series of increasing X-ray exposures in the microsecond time range as previously described (Fig 3a)(17). High-resolution quantitative bottom-up LCMS provided a residue-specific dose response for each site of modification and covered nearly all regions of the protein domains. The pseudo-first-order fit of the dose-response gives the hydroxyl radical reactivity rate constant (k s^{-1}), which is a measure of both intrinsic reactivity and SA of the modified side chain (Fig. S5 to S10). In the comparative structural analysis, the ratio (R) of rate constants between samples determines the relative SA changes, which are independent of any sequence context (8,17). FRP binding may also induce protein conformational changes associated with an increase (R > 1) or decrease (R < 1) in SA of certain residues. In our study, we considered a more than 3-fold change in accessibility as

significant and indicative of binding and/or conformational change (Fig. 3b-d and Table S3).

To obtain a comprehensive view of the interaction of the OCP with the FRP we compared the reactivity rate of an equimolar molar concentration of OCP^O and OCP^R to that of the OCP-FRP complexes under dark (OCP^O-FRP) and light illuminated (OCP^R-FRP) conditions (Fig 3b and c). Notably, we observed strong protection (R<0.2) of OCP residues Pro276, Trp277, Phe278 and Met284 for both the dark and light illuminated complexes. Also, binding of FRP to the CTD alone resulted in marked protection of residue Met284 (Fig 3d). We summarize that this high degree of protection is due to the presence of a stable and bound FRP to both OCP^O and OCP^R during the time course of microsecond X-ray irradiation. While the protection of these residues indicates binding of FRP at the major interface, the SA of residues Arg155-Asn156 increases > 3-fold in the dark complex, but not in the light illuminated complex. The reactivity of these residues in OCP^O and OCP^R is consistent with previous XFMS studies on the photoactivation of OCP showing that Arg155, in particular, becomes more solvent accessible during the OCP^O to OCP^R transition (Fig. S4 and S5) (8). Addition of FRP has no effect on the SA of Arg155-Asn156 in the light illuminated complex when the domains are already separated, but does increase flexibility of Arg155-Asn156 in the dark-adapted complex, which is consistent with a model of FRP binding to the CTD half of the major interface, thereby displacing the NTD and increasing Arg155 solvent exposure. The residues in the region 13-22, in contrast, increases in SA > 3-fold in both dark and light complexes. Recently, it was suggested through mutation and spectroscopic studies that a region of FRP binds to OCP at the minor interface (14). In this model, an FRP N-terminal segment of approximately ten residues displaces the NTD αA of OCP. Our observation of an increase in accessibility of residues 13-22, which is adjacent to NTD αA of OCP, suggests that FRP binding occurs on an extended surface area of both FRP and OCP that might cause a displacement of the helical region adjacent to OCP residues 13-22. We also observe that, although protection of FRP during binding to OCP covers a large area, the >2-fold protection consistently resides only on peptide 71-83, which forms the head region of FRP (Fig 4a and b, Table S4), consistent with recent studies showing substitution of Phe76 in FRP severely affects FRP-OCP interaction (5,15). In the light-illuminated complex, the near 2-fold protection is extended to the N-terminal peptide, whereas in the dark and CTD-FRP complex it shows either no overall change (Fig 4a) or a slight increase, respectively (Fig 4c). The rest of the FRP segments show similar protection in all complexes. The high degree of protection at the head region is likely due to its binding to the CTD, whereas the variable protection pattern in the N-terminal segment of FRP might be caused by the dynamic interaction of the FRP with OCP.

The rate of hydroxyl radical reactivity of the OCP residues implicated in binding to FRP did not change when the FRP concentration was increased from 1 to 5-fold in excess, suggesting that the OCP binding site was saturated with FRP (Fig 4d and Fig. S11). In contrast, the hydroxyl radical reactivity of the OCP binding sites on the FRP gradually reversed to the original values as molar excess of FRP increased, indicating the presence of unbound FRP (Fig 4d). These results are corroborated by studies on the stoichiometry of FRP-OCP complexes using size exclusion chromatography and mutational analysis, which found that OCP likely recruits dimeric FRP, but that further rearrangement is accompanied by FRP monomerization, possibly because OCP domain reassociation disrupts the FRP dimer, and that carotenoid motion occurs after FRP monomerization (15).

Discussion

Physiological relevance of hysteresis in the photoactivation and relaxation processes

Time-resolved XFMS showed that the OCP photoactivation and relaxation processes occur through different pathways. Under constant illumination the activation process is characterized by single phase kinetic profiles,

though with subtle residue-specific rate differences in which the fastest SA changes are confined to prominent carotenoid binding residues in the carotenoid binding pocket, followed by SA changes at the inter-domain interface. Since XFMS is highly sensitive to any change in a protein-water network (18), our data also show that the reorganization of the carotenoid environment and carotenoid translocation directly influence the accessibility of local bound and conserved waters, which are present adjacent to the carotenoid cavity and domain interface (8). The destabilization of the carotenoid environment associated with several aromatic residues in the hydrophobic carotenoid binding pockets was shown as the initial photoactivation event by dynamics crystallography and single crystal microspectrometry (9), and in addition, recent kinetics studies have shown that during photoactivation, carotenoid movement precedes domain rearrangement by over two decades of time (19). However, it has been previously shown that water molecules can also play an important role in hydrophobic and ionic interactions to define the shape of protein cavities (20,21). Therefore, although XFMS could not directly probe changes on those buried aromatic residues, it identified additional residues, directly or indirectly connected to the H-bonding network involving conserved water at the carotenoid binding pocket undergoing conformational changes during the initial event of the photoactivation process (8) and chromophore migration (22). In contrast to the dynamic crystallography study, we observed the slowest conformational transition at the NTD αA. The discrepancy could be due to either the influence of continual back conversion to OCP^O in solution or the inherent structural difference between the monomeric OCP in solution versus the strongly associated antiparallel dimeric form in the crystal. Overall our data indicated the carotenoid migration first destabilizes the water-protein network at the major interface, which then drives the overall structural reorganization and domain dissociation, thus propagating the signal from the active site to the protein surface.

Previous reports showed that the initial rate of photoactivation is temperature independent and the overall process is ionic strength dependent (12,23). SA measurements by XFMS studies on *Arthrospira* OCP, an ortholog of *Synechocystis* OCP, showed that an increase in salt concentration affects local protein-water interactions which are critical for maintaining the native OCP^O state (Fig. S4). The residues at the major and minor interfaces are tightly packed through an extensive H-bonding network between sidechains and bound water (8). As shown earlier, this dense hydration layer connects both buried water clusters at the carotenoid cavity and the surface-bound waters at the major and minor interfaces (8). It is possible that water, both as part of bound water clusters and as part of the hydration layer, can mitigate local conformational fluctuations around the carotenoid cavity resulting from temperature changes by a mechanism similar to thermophilic proteins (20,24,25). This can make the initial stage of the photoactivation process strictly driven by the intensity of the light and thus providing a very specific and directional driving force for the signal transfer from the carotenoid to the protein surface. Such temperature independence might provide a way for the organism to induce photo-protection by the intensity of light as the single controlling factor.

The relaxation process showed generally multiphasic kinetic profiles in which the first step involved the formation of a compact intermediate and exclusion of water. While previous reports (12) using time-resolved fluorescence static quenching measurements indicated the formation of a distinct orange intermediate before the final structural rearrangement, our study pinpointed residue-specific information characteristic of the intermediate state. The domain association and re-structuring of conserved water-protein interactions at the major and minor interface appear faster than the final rearrangements at the carotenoid pocket residues and the minor structural rearrangements throughout the entire protein in the process of returning to the native OCP^O conformation. At the same time, since the OCP^O and OCP^R are always at

equilibrium, the fast domain association in the reverse process can contribute to the slower rate of the forward process that we observed under constant illumination. It is likely that the overall rate will depend on the temperature, as indicated in previous UV-visible progress curves (26). The entire relaxation process is indeed highly temperature dependent, suggesting that the compact intermediate might represent one of the local conformational energy minima along the pathway to formation of the final OCP^O state. In this view, the relaxation process is a kinetically controlled process in which a decrease in temperature can trap the conversion to a local minimum or a misfolded state as observed by time-resolved XFMS at 4°C (Fig 2a and Fig. S3). It has previously been shown that the activation entropy for the OCP-FRP relaxation process is significantly lower than for the un-aided relaxation of OCP^R to OCP^O (14). This is consistent with our interpretation of the data, which reveal the presence of an unfavorable intermediate in the absence of FRP; FRP binding may serve to eliminate this intermediate and thus accelerate the back-conversion to the final conformation of OCP^O.

Mode of FRP-OCP interactions

XFMS confirms that FRP binds to CTD at the major interface as well as interacts at the minor interface at equimolar concentration. We performed docking simulations with XFMS-based constraints to generate a model of the OCP-FRP complex. The crystal structure of the FRP shows that the protein can exist in two conformations with distinct oligomeric states, a dimer with a folded helix at the N-terminal half, and a tetramer with a long extended helix (5). The tetramer is not prominently observed in solution and another recent crystal structure consisted of the dimer only (27). Docking simulations used the FRP's head region (residues 54-109) from the FRP-dimer, and the FRP-tetramer crystal structure with the full-length OCP without carotenoid or the isolated C-terminal domain. The most acceptable solution indicated by a narrow funnel in a rmsd vs. interface energy plot (Fig. S12) was obtained from a complex of the FRP head domain originating from the dimer with the OCP-CTD. Our model indicates that the conserved head region remained intact and interacted with the CTD. The head region of FRP binds at the major interface, protecting residues Pro276, Trp277, Phe278 and Met284. Specifically, a hydrophobic binding interface exists with Leu81 and Leu86 of FRP surrounding Met284 of OCP-CTD that show marked protection upon FRP binding (Fig 5a). When we use the FRP head domain – CTD complex as a template and fit the full chain of the FRP dimer, the α1 helix clashes with the CTD (Fig. 5b). However, a rotation of the α1 helix by about 50 degrees (Fig. 5c) would alleviate the clash and we used such a template as a starting point for a docking simulation. The resulting complex is energetically favorable, indicating that such an interaction would be possible. This type of rotation of α1 is also very likely to occur for FRP in solution since it is a prerequisite for the formation of the tetramer form with a long extended helix (a fusion of α1 and α2) observed in the crystal structure.

The FRP α1 helix in this complex is located where the NTD αA helix of OCP is located in OCP^O, consistent with previous results that suggest that FRP can bind in that region (14). However, in our complex a different region of FRP (residues 36-40 vs 12-21 in (14)) is in the location where NTD αA is in OCP^O. Such an extensive mode of binding requires conformational changes in the helical regions of the N-terminal half of the FRP. The slight increase of SA in the N-terminal helix of FRP in the presence of CTD might be due to the conformation change from a folded N-terminal half helical segment to a more elongated one. In contrast, a slight decrease in the SA of the FRP α1 helix in the presence of OCP^R indicates a relatively stable interaction of the elongated α1 helix with the CTD in OCP^R. The overall change and a high degree of fluctuation in the SA of the α1 helix in the presence of OCP^O suggests a dynamic nature of the interaction, which is plausible because of the presence of the NTD αA in OCP^O. The structure of FRP is known to be flexible, evident by the two very different forms observed in the same crystal, so an influence

of the OCP/CTD on the structure of FRP that is connected to its function is quite likely (5,28). It has also been previously suggested that the FRP acts as a scaffold for OCP domain reassociation (14). Our model indicates that the extended form of FRP binding may bring the two domains of the OCP close to each other, reducing their motion, so that they can efficiently sample different structural configurations and provide an environment conducive to carotenoid movement. Scaffolding by FRP might help order water clusters along the major interface; interdomain interactions between conserved residues and bound water have been shown to be important for proper domain association (8). Formation of the correct H-bonding network, in turn, might facilitate the formation of H-bonds between the carbonyl group of β-ring of the carotenoid and Y201 and W288. Noticeably, many residues in the cavity surrounding the carotenoid showed a slightly higher SA in the presence of FRP - in particular, residues Trp41, Tyr44, Met47, Met161, Phe163 - in the OCP-FRP complex compared to OCP^O (Fig 3b and c). This indicates that FRP binding may also induce some flexibility in the carotenoid environment and the large cavity at the major interface and prevent any drastic change in a conformation such as compaction in the absence of FRP. An overall model of the OCP photocycle, including the compact intermediate, is shown in Fig 6.

Recently, new paralogous OCP families have been discovered in cyanobacteria (27). For example, the cyanobacterium *Tolypothrix* sp. PCC 7601 encodes two distinct forms of the OCP. OCP1, the canonical OCP, is functionally equivalent to the *Synechocystis* OCP. In contrast, OCP2, a new family, exhibits both faster photoactivation and back-conversion, is less temperature sensitive, and FRP does not influence its dark reversion. Given that FRP may act as a scaffold to accelerate back-conversion of OCP1, it is interesting to compare the differences in primary structure between OCP1 and OCP2 (Fig. S13). One of the key sequence differences between OCP2 and OCP1 is the substitution of isoleucine for methionine in position 284. In the OCP1 photoactivated form, the residue Met284 becomes highly accessible, and during relaxation in the presence of FRP, it forms a rapid compact or misfolded intermediate. In the orange form, residue Met284 resides very close to the conserved water cluster and the carotenoid at the major interface. Methionine residues are unique in the protein core as they can have hydrophobic interactions while also engaging in polar contacts (6,29-31). The presence of isoleucine might eliminate the requirement for FRP to bind and assist the formation of the correct polar contacts at the major interface involving water clusters. Two other critical differences -- the substitution Tyr240 to Phe240, and the substitution Lys/Arg for Glu229 -- might have a direct influence on the non-FRP relaxation of OCP2. Phe240 in OCP1 is located close to the β–keto group of the carotenoid in the CTD and a tyrosine at the same position further stabilizes the carotenoid by H-bond formation. Lys/Arg229 in OCP1 is projected towards Arg9 and participates in H-bonding to stabilize the αA-CTD interaction at the minor interface. Arg9 is involved in an H-bonding network with water clusters at the minor interface which in turn connects several functionally important residues such as Arg155 (NTD) and Phe227 (CTD). The substitution of Arg229 by Glu229 might further strengthen the domain interaction at the minor interface further by electrostatic stabilization. Overall in the OCP2, substitution of several conserved residues might have led to a more rapid sampling of the domain interface to form the correct geometry of the dark-adapted conformation in the absence of FRP. Recent studies (3) have pinpointed OCP residues Phe299 and Asp220 as playing an important role in the acceleration of the relaxation process in the presence of FRP. Although this study did not explicitly show a change in accessibility of these residues upon FRP binding - likely because the residues are in proximity to water molecules in both the bound and un-bound FRP forms - it is interesting to note that they are in the region in which the N-terminal extension of the FRP binds in the scaffolding model (Fig. 5).

Conclusion

In this study, X-ray radiolytic labeling revealed new mechanistic details of the key events in OCP photoprotection, providing both a spatial and temporal view of site-specific conformational changes in the OCP and its interaction with the FRP. By temporally differentiating residue-specific SA changes we have determined the driving force for photoactivation and relaxation under native conditions by pinpointing the sequence of structural events during these processes. We determined that FRP provides an extended binding region which effectively holds together the OCP domains at the major and minor interfaces, and forces proximity of the two domains to lead to the acceleration of OCP^R relaxation to OCP^O. Together, these data allowed the construction of a molecular model of the FRP binding process and its role in the regulation of the OCP. Recent studies have suggested that the OCP-CTD is accessible when OCP is bound to the PB (32), and therefore future studies will include investigating the role of FRP in detaching OCP from the OCP-PB complex. Studying residue-specific kinetics of water accessibility changes in OCP^R in the presence of the FRP, and as a function of OCP binding to PB will generate a more complete understanding of the driving force underlying the NPQ mechanism in cyanobacteria. Understanding the switching on and off of thermal dissipation, and the action of the 'photoswitch' which controls this mechanism has long-ranging implications in synthetic biology, such as design of optogenetic switches (33) or the finer control of photoprotection and consequent enhancement of photosynthetic efficiency (34).

Experimental Procedures

Purification of OCP, FRP, and CTD

OCP and FRP samples were purified using procedures described previously (5,8). CTD preparations incorporating Canthaxanthin (CAN) were obtained by expressing the gene for Synechocystis sp. PCC 6803 in BL21(DE3) competent Escherichia coli cells with 6X His tag added. BL21(DE3) cells were transformed simultaneously with the pCDFDuet-1 vector and the pAC-CANTHipi plasmid (Addgene plasmid # 53301)36 containing the genes enabling CAN biosynthesis in *E. coli*. The CTD_{CAN} holoprotein was isolated by Ni-NTA affinity chromatography (HisTrap Affinity column, GE Healthcare) yielded a mixture of apo- and holoproteins. The CTD-CAN holoprotein was further isolated by hydrophobic interaction chromatography (HiTrap HIC phenyl column, GE Healthcare). The purity of the final OCP fractions was confirmed by SDS-PAGE. The protein samples were exchanged into 20 mM potassium phosphate (pH 7.4), 100 mM NaCl by Size Exclusion Chromatography (SEC) on a Superdex-75 10/300 GL column prior to XFMS experiments.

Time-dependent XFMS measurements to follow OCP photoactivation and relaxation

The OCP_{ECN} (expressed in *Synechocystis* PCC 6803) samples were exchanged into 20 mM potassium phosphate (pH 7.4), 100 mM NaCl by SEC on a Superdex-75 10/300 GL column prior to XFMS experiments. Based on UV-visible spectrometry measurements of OCP photoactivation and deactivation, the time window to follow the conformation transition by XFMS is set to a range of "zero" to 30 min. To follow the photoactivation pathway, 2.5 ml of OCP^O inside the sample loading syringe of microfluidic flow system was illuminated with a blue LED array (470 nm Luxeon Rebel, Philip Lumileds) at room temperature for 30 min. At various intervals (delay time) within this duration of the LED illumination, 200 μl sample was passed through a 200 μm I.D. Polymicro® capillary tube and 200 X 500 μm^2 beam spot to receive a 200 μs of X-ray exposure at beamline 5.3.1 at the Advanced Light Source (17). The "zero" time interval sample was collected at the beginning under dark conditions. All samples were immediately quenched with methionine amide to stop the secondary oxidations and stored at -80 °C for LCMS analysis. To follow the time course of the reverses pathway, which is the decay of OCP^R to OCP^O, 2.5 ml of OCP_{ECN} sample was first illuminated inside the sample loading syringe of a microfluidic flow system for 15 min at room temperature to

prepare OCP^R. The LED was then turned off, and at various intervals, 200 μl of sample was exposed to X-ray as described above. The "zero" time interval of the reverse transition was collected at the beginning in the presence of LED illumination. In both forward and backward transitions, we were able to collect the first data point only at ~ 40 sec because of the inherent delays associated with a manual operation of beamline components and sample handling system.

Steady-state XFMS measurements to study interaction of FRP with OCP and CTD

The steady-state XFMS were carried out at the Advanced Light Source beamline 5.3.1 using a standard microfluidic set-up (8,17). All protein samples (OCP^O, OCP^R, OCP^O-FRP, OCO^R-FRP, CTD, FRP, and CTD-FRP) at 5 μM concentration in 20 mM potassium phosphate (pH 7.4) buffer containing 100 mM NaCl were subject to X-ray exposure from 0 to 800 μs, and immediately quenched with methionine amide to stop the secondary oxidations and stored at -80 °C for LCMS analysis. The sample handling and exposure of OCP^O-FRP and OCO^R-FRP complex were carried out under dark and light illuminated conditions respectively. The protein complexes OCP-FRP and CTD-FRP were prepared at 5 μM concentration by mixing equimolar ratio of individual protein components. Additionally, the OCP^R-FRP complex at various amount of molar excess of FRP (1, 2, and 5-fold) was exposed to monitor the effect of a molar excess of FRP on SA changes at the binding sites. The SA changes are proportional to the reactivity rates, which rates have been corrected for the scavenging effect of the excess amount of FRP determined by the standard Alexa 488 assay (35).

Mass spectrometry and data analysis

The pH of the exposed samples were increased to pH 8 by ammonium bicarbonate to a final concentration of 50 mM. The disulfide linkages in the protein samples were reduced by treatment with DTT to a final concentration of 5 mM and incubating at 55°C for 30 min. The Cys residues were alkylated by treating the samples with iodoacetamide to a final concentration of 15 mM at room temperature and in the dark for 30 min. The cys-alkylated proteins were then de-salted and buffer exchanged with 50 mM ammonium biocarbonate pH 8 using Zeba™ desalting spin columns (Thermo Fisher Scientific). Samples were digested overnight with trypsin (1:20 weight/weight, enzyme:protein) and endoproteinase GluC (1:10 weight/weight, enzyme:protein) at pH 8 and 37°C. Proteolyzed samples were analyzed in an Agilent 6550 iFunnel Q-TOF mass spectrometer (Agilent Technologies, Santa Clara, CA) coupled to an Agilent 1290 LC system (Agilent) using Sigma-Aldrich Ascentis Peptides ES-C18 reverse phase column (2.1 mm x 100 mm, 2.7 μm particle size; Sigma-Aldrich, St. Louis, MO). Approximately 10 pmol of samples were loaded onto the column via an Infinity Autosampler (Agilent) with Buffer A (2% Acetonitrile, 0.1% Formic Acid) flowing at 0.400 mL/min. The peptides were separated and eluted into the mass spectrometer via a gradient with initial condition of 5% buffer B (98% Acetonitrile, 0.1% Formic Acid) increasing to 70% B over 15 minutes. Subsequently, B was increased to 90% over 1 minute and held for 3 minutes at a flow rate of 0.6 ml/min followed by a ramp back down to 5% over 1 minute where it was held for minutes to re-equilibrate the column to the original condition. Peptides were introduced to the mass spectrometer from the LC using a Jet Stream source (Agilent) operating in positive-ion mode (3500 V). The data were acquired with MassHunter B.05.00 operating in Auto MS/MS mode whereby the three most intense ions (charge states 2 - 5) within 300 m/z to 1400 m/z mass range above a threshold of 1000 counts were selected for MS/MS analysis. MS/MS spectra were collected with the quadrupole set to "Narrow" resolution and collision energy to optimize fragmentation. MS/MS spectra were scanned from m/z 100 to 1700 and were collected until 40000 total counts were collected or for a maximum accumulation time of 333 ms. Parent ions were excluded for 0.1 minutes following MS/MS acquisition. MS/MS data of native and modified peptide fragments were interpreted by Mascot

MS/MS Ions Search as well as verified manually. The abundance of native and modified peptides at any irradiation time point area were measured (peak area) from their respective extracted ion chromatogram using Agilent Mass Hunter v 2.0.

The peak area from the extracted ion chromatograms of a specific peptide fragment with a particular mass-to-charge ratio and associated +16, +32 or +48 Da side-chain modifications was used to quantify the amount of modification at yielded at 200 μs of exposure time for time-resolved studies. The increase in delay time progressively reduces or increases the fraction of the unmodified product. The plot of fraction unmodified versus delay time provides a site-specific kinetic trace. The multiple experimental repeats of the kinetic traces are fitted globally to an exponential decay function with Origin version 6.1 (OriginLabs®) to determine the lifetime (τ) of conformational change. The reported errors of the rate data were determined by the Origin program using 95% confidence limits of the fitting results.

For FRP binding studies the peak area from the extracted ion chromatograms of a specific peptide fragment with a particular mass-to-charge ratio and associated +16, +32 or +48 Da side-chain modifications was used to quantify the amount of modification at a given irradiation time. Increasing irradiation progressively reduces the fraction of unmodified products and provides a site-specific dose-response plot (17,22). The hydroxyl radical reactivity rate (k), which depends on both intrinsic reactivity and SA, was obtained by fitting the dose response to a single exponential decay (based on a pseudo-first-order reaction scheme using Origin 7.5 (OriginLabs®) (Fig. S5 to S11). The ratio (R) of the measured reactivity of the side chains residues between free protein and bound complex ($R = k_{bound} / k_{free}$) gave information on SA changes independent of the intrinsic reactivity (Table S3 and S4).

Docking Simulations

XFMS-based restraints were used to generate the starting positions of the docking partners using PatchDock (36). These starting positions of the docking partners were then uploaded to RosettaDock (37). 1000 independent simulations were performed and the 10 best-scoring structures were returned at the end of the simulation. One of those solutions was then used for a refinement run with RosettaDock (10'000 structures) with standard deviation perturbation parameters of 4 Å for translation and 6 degreed for rotation. The energetic 'funnel' with low energy structures clustered around a single position with minimal rmsd was obtained (Fig. S12). The model of full-length FRP with a rotated α1 helix was generated based on the full-length FRP dimer with a manually rotated helix that was subsequently relaxed with RosettaRelax and then used for docking. Simulations with full-length OCP and FRP as well as combinations without restraints did not indicate successful runs. Structures were visualized in PyMol 2.0 (Schrodinger) and Chimera (38).

Acknowledgments

The Kerfeld Lab (CAK, HB, MAD-M, MS) acknowledges the support of the National Science Foundation (IOS 1557324) and infrastructure support by the U.S. Department of Energy, Basic Energy Sciences, contract DE-FG02-91ER20021. The XFMS was supported in part by NIH 1R01GM126218, and conducted at the Advanced Light Source and Joint BioEnergy Institute, supported by the Office of Science, Office of Biological and Environmental Research, of the U.S. DOE under contract DE-AC02-05CH11231. We also acknowledge Jun Feng for experimental help at beamline 5.3.1, and Emily G. Pawlowski for assistance in purifying the OCP. The authors declare that they have no conflict of interest.

Conflict of interest

The authors declare that they have no conflicts of interest with the contents of this article

References

1. Muller, P., Li, X. P., and Niyogi, K. K. (2001) Non-photochemical quenching. A response to excess light energy. *Plant Physiol* **125**, 1558-1566
2. Kirilovsky, D., and Kerfeld, C. A. (2016) Cyanobacterial photoprotection by the orange carotenoid protein. *Nat Plants* **2**, 16180
3. Thurotte, A., Bourcier de Carbon, C., Wilson, A., Talbot, L., Cot, S., Lopez-Igual, R., and Kirilovsky, D. (2017) The cyanobacterial Fluorescence Recovery Protein has two distinct activities: Orange Carotenoid Protein amino acids involved in FRP interaction. *Biochim Biophys Acta* **1858**, 308-317
4. Boulay, C., Wilson, A., D'Haene, S., and Kirilovsky, D. (2010) Identification of a protein required for recovery of full antenna capacity in OCP-related photoprotective mechanism in cyanobacteria. *Proc Natl Acad Sci U S A* **107**, 11620-11625
5. Sutter, M., Wilson, A., Leverenz, R. L., Lopez-Igual, R., Thurotte, A., Salmeen, A. E., Kirilovsky, D., and Kerfeld, C. A. (2013) Crystal structure of the FRP and identification of the active site for modulation of OCP-mediated photoprotection in cyanobacteria. *Proc Natl Acad Sci U S A* **110**, 10022-10027
6. Kerfeld, C. A., Sawaya, M. R., Brahmandam, V., Cascio, D., Ho, K. K., Trevithick-Sutton, C. C., Krogmann, D. W., and Yeates, T. O. (2003) The crystal structure of a cyanobacterial water-soluble carotenoid binding protein. *Structure* **11**, 55-65
7. Wilson, A., Kinney, J. N., Zwart, P. H., Punginelli, C., D'Haene, S., Perreau, F., Klein, M. G., Kirilovsky, D., and Kerfeld, C. A. (2010) Structural determinants underlying photoprotection in the photoactive orange carotenoid protein of cyanobacteria. *J Biol Chem* **285**, 18364-18375
8. Gupta, S., Guttman, M., Leverenz, R. L., Zhumadilova, K., Pawlowski, E. G., Petzold, C. J., Lee, K. K., Ralston, C. Y., and Kerfeld, C. A. (2015) Local and global structural drivers for the photoactivation of the orange carotenoid protein. *Proc Natl Acad Sci U S A* **112**, E5567-5574
9. Bandara, S., Ren, Z., Lu, L., Zeng, X., Shin, H., Zhao, K. H., and Yang, X. (2017) Photoactivation mechanism of a carotenoid-based photoreceptor. *Proc Natl Acad Sci U S A* **114**, 6286-6291
10. Leverenz, R. L., Jallet, D., Li, M. D., Mathies, R. A., Kirilovsky, D., and Kerfeld, C. A. (2014) Structural and functional modularity of the orange carotenoid protein: distinct roles for the N- and C-terminal domains in cyanobacterial photoprotection. *Plant Cell* **26**, 426-437
11. Berera, R., van Stokkum, I. H., Gwizdala, M., Wilson, A., Kirilovsky, D., and van Grondelle, R. (2012) The photophysics of the orange carotenoid protein, a light-powered molecular switch. *J Phys Chem B* **116**, 2568-2574
12. Maksimov, E. G., Shirshin, E. A., Sluchanko, N. N., Zlenko, D. V., Parshina, E. Y., Tsoraev, G. V., Klementiev, K. E., Budylin, G. S., Schmitt, F. J., Friedrich, T., Fadeev, V. V., Paschenko, V. Z., and Rubin, A. B. (2015) The Signaling State of Orange Carotenoid Protein. *Biophys J* **109**, 595-607
13. Niedzwiedzki, D. M., Liu, H., and Blankenship, R. E. (2014) Excited state properties of 3'-hydroxyechinenone in solvents and in the orange carotenoid protein from Synechocystis sp. PCC 6803. *J Phys Chem B* **118**, 6141-6149
14. Sluchanko, N. N., Klementiev, K. E., Shirshin, E. A., Tsoraev, G. V., Friedrich, T., and Maksimov, E. G. (2017) The purple Trp288Ala mutant of Synechocystis OCP persistently quenches phycobilisome fluorescence and tightly interacts with FRP. *Biochim Biophys Acta* **1858**, 1-11
15. Slonimskiy, Y. B., Maksimov, E. G., Lukashev, E. P., Moldenhauer, M., Jeffries, C. M., Svergun, D. I., Friedrich, T., and Sluchanko, N. N. (2018) Functional interaction of low-homology FRPs from different cyanobacteria with Synechocystis OCP. *Biochim Biophys Acta* **1859**, 382-393

16. Xu, G., and Chance, M. R. (2007) Hydroxyl radical-mediated modification of proteins as probes for structural proteomics. *Chem Rev* **107**, 3514-3543
17. Gupta, S., Chai, J., Cheng, J., D'Mello, R., Chance, M. R., and Fu, D. (2014) Visualizing the kinetic power stroke that drives proton-coupled zinc(II) transport. *Nature* **512**, 101-104
18. Gupta, S., Feng, J., Chan, L. J., Petzold, C. J., and Ralston, C. Y. (2016) Synchrotron X-ray footprinting as a method to visualize water in proteins. *J Synchrotron Radiat* **23**, 1056-1069
19. Konold, P. E., van Stokkum, I. H. M., Muzzopappa, F., Wilson, A., Groot, M. L., Kirilovsky, D., and Kennis, J. T. M. (2018) Photoactivation mechanism, timing of protein secondary structure dynamics and carotenoid translocation in the Orange Carotenoid Protein. *J Am Chem Soc* **141**, 520-530
20. Chakraborty, D., Taly, A., and Sterpone, F. (2015) Stay Wet, Stay Stable? How Internal Water Helps the Stability of Thermophilic Proteins. *Journal of Physical Chemistry B* **119**, 12760-12770
21. Breiten, B., Lockett, M. R., Sherman, W., Fujita, S., Al-Sayah, M., Lange, H., Bowers, C. M., Heroux, A., Krilov, G., and Whitesides, G. M. (2013) Water networks contribute to enthalpy/entropy compensation in protein-ligand binding. *J Am Chem Soc* **135**, 15579-15584
22. Leverenz, R. L., Sutter, M., Wilson, A., Gupta, S., Thurotte, A., Bourcier de Carbon, C., Petzold, C. J., Ralston, C., Perreau, F., Kirilovsky, D., and Kerfeld, C. A. (2015) PHOTOSYNTHESIS. A 12 A carotenoid translocation in a photoswitch associated with cyanobacterial photoprotection. *Science* **348**, 1463-1466
23. Wilson, A., Punginelli, C., Gall, A., Bonetti, C., Alexandre, M., Routaboul, J. M., Kerfeld, C. A., van Grondelle, R., Robert, B., Kennis, J. T., and Kirilovsky, D. (2008) A photoactive carotenoid protein acting as light intensity sensor. *Proc Natl Acad Sci U S A* **105**, 12075-12080
24. Sterpone, F., Bertonati, C., Briganti, G., and Melchionna, S. (2010) Water around thermophilic proteins: the role of charged and apolar atoms. *J Phys-Condens Mat* **22**
25. Melchionna, S., Sinibaldi, R., and Briganti, G. (2006) Explanation of the stability of thermophilic proteins based on unique micromorphology. *Biophys J* **90**, 4204-4212
26. Sluchanko, N. N., Slonimskiy, Y. B., Shirshin, E. A., Moldenhauer, M., Friedrich, T., and Maksimov, E. G. (2018) OCP-FRP protein complex topologies suggest a mechanism for controlling high light tolerance in cyanobacteria. *Nat Commun* **9**, 3869
27. Bao, H., Melnicki, M. R., Pawlowski, E. G., Sutter, M., Agostoni, M., Lechno-Yossef, S., Cai, F., Montgomery, B. L., and Kerfeld, C. A. (2017) Additional families of orange carotenoid proteins in the photoprotective system of cyanobacteria. *Nat Plants* **3**, 17089
28. Sali, A., and Blundell, T. L. (1993) Comparative protein modelling by satisfaction of spatial restraints. *J Mol Biol* **234**, 779-815
29. Pal, D., and Chakrabarti, P. (2001) Non-hydrogen bond interactions involving the methionine sulfur atom. *J Biomol Struct Dyn* **19**, 115-128
30. Biswal, H. S., Gloaguen, E., Loquais, Y., Tardivel, B., and Mons, M. (2012) Strength of (NHS)-S-... Hydrogen Bonds in Methionine Residues Revealed by Gas-Phase IR/UV Spectroscopy. *J Phys Chem Lett* **3**, 755-759
31. Reddi, R., Singarapu, K. K., Pal, D., and Addlagatta, A. (2016) The unique functional role of the C-H center dot center dot center dot S hydrogen bond in the substrate specificity and enzyme catalysis of type 1 methionine aminopeptidase. *Mol Biosyst* **12**, 2408-2416
32. Harris, D., Tal, O., Jallet, D., Wilson, A., Kirilovsky, D., and Adir, N. (2016) Orange carotenoid protein burrows into the phycobilisome to provide photoprotection. *Proc Natl Acad Sci U S A* **113**, E1655-1662
33. Shcherbakova, D. M., Shemetov, A. A., Kaberniuk, A. A., and Verkhusha, V. V. (2015) Natural photoreceptors as a source of fluorescent proteins, biosensors, and optogenetic tools. *Annu Rev Biochem* **84**, 519-550

34. Leonelli, L., Brooks, M. D., and Niyogi, K. K. (2017) Engineering the lutein epoxide cycle into Arabidopsis thaliana. *Proc Natl Acad Sci U S A* **114**, E7002-E7008
35. Gupta, S., Bavro, V. N., D'Mello, R., Tucker, S. J., Venien-Bryan, C., and Chance, M. R. (2010) Conformational changes during the gating of a potassium channel revealed by structural mass spectrometry. *Structure* **18**, 839-846
36. Wang, C., Bradley, P., and Baker, D. (2007) Protein-protein docking with backbone flexibility. *J Mol Biol* **373**, 503-519
37. Schneidman-Duhovny, D., Inbar, Y., Nussinov, R., and Wolfson, H. J. (2005) PatchDock and SymmDock: servers for rigid and symmetric docking. *Nucleic Acids Res* **33**, W363-367
38. Pettersen, E. F., Goddard, T. D., Huang, C. C., Couch, G. S., Greenblatt, D. M., Meng, E. C., and Ferrin, T. E. (2004) UCSF chimera - A visualization system for exploratory research and analysis. *J Comput Chem* **25**, 1605-1612

Abbreviations and nomenclature

NPQ nonphotochemical quenching; OCP Orange Carotenoid Protein; OCP^O (orange) inactive (non-quenching) state of the OCP; OCP^R (red) activated (quenching) state of the OCP; PB phycobilisome; XFMS X-ray hydroxyl radical footprinting coupled with mass spectrometry; FRP fluorescence recovery protein; OCP_{ECN} Orange Carotenoid Protein containing echinenone carotenoid; CTD_{CAN} C-terminal Domain of OCP containing canthaxanthin carotenoid; SA solvent accessibility.

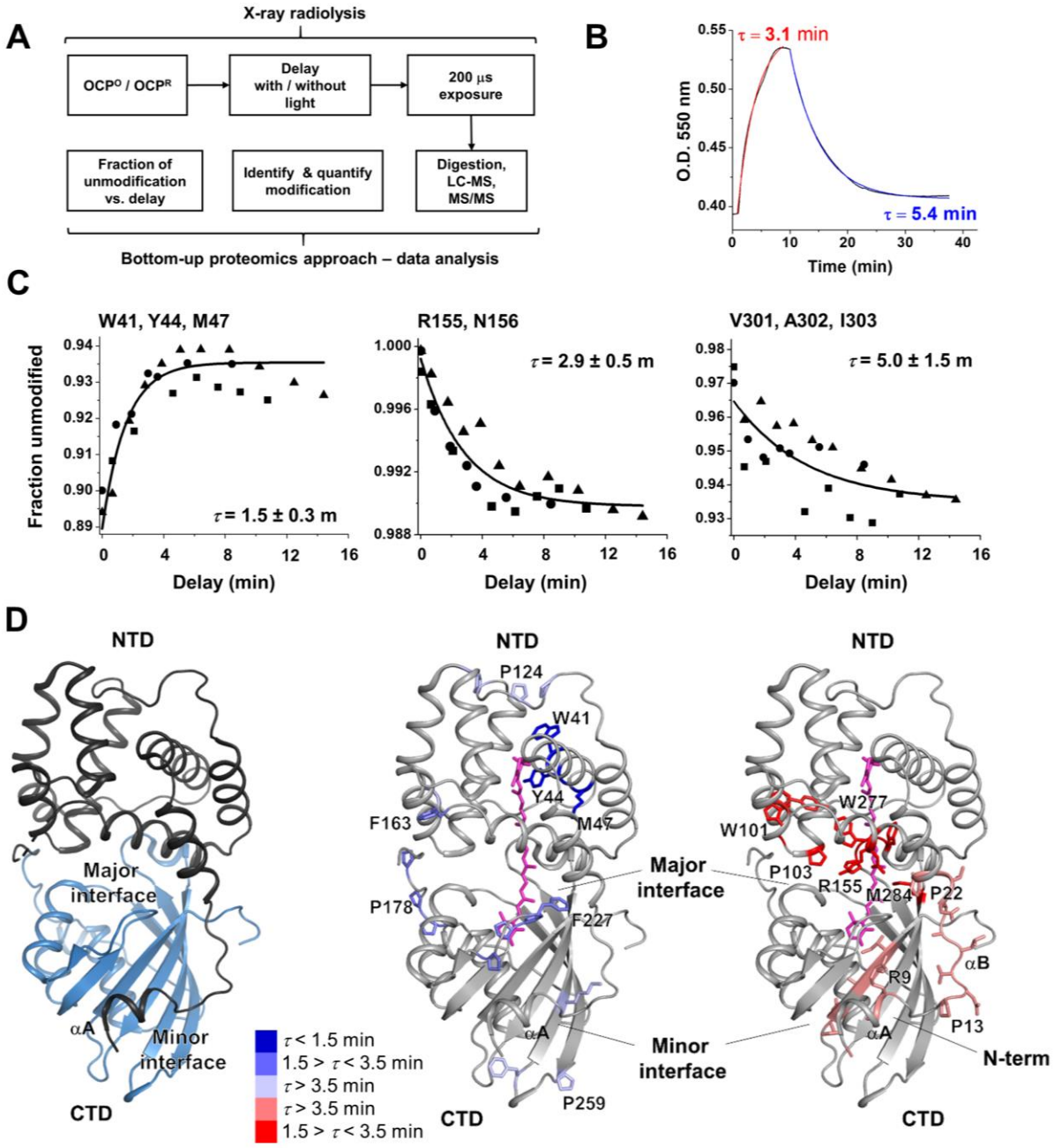

Figure 1. Time-evolution of local conformational changes in OCP^O photoactivation
(A) Overall experimental scheme to monitor OCP photoactivation and relaxation by XFMS in real time. (B) UV-visible kinetic traces for the photoactivation and relaxation of OCP at 15 °C, obtained just prior to XFMS experiments. Red and blue solid line represents the single exponential fit of the time course of change in OD at 550 nm. (C) Representative time-resolved SA progress curves for the photoactivation process**.** Residues W41, Y44 and M47 are in the carotenoid binding pocket within the NTD. Residues R155N156 are located at the domain interface between the N- and C-terminal domains of OCP. Residues V301, A302, and I303 are located near the N-terminal α–helix. The solid line represents a single exponential fit of the time course of the unmodified fraction with a fitted lifetime (τ) from three independent measurements (closed circles, squares

and triangles). (D) On the left is the structure of the OCP^O (PDB ID 3MG1), showing the domains and their interfaces. The residues from the three categories (Table S1) are mapped onto the OCP^O structure. Carotenoid is in purple, residues in blue show a SA decrease upon activation, and those in red show an increase. The speed of decrease or increase is indicated by lifetime and the depth of the color.

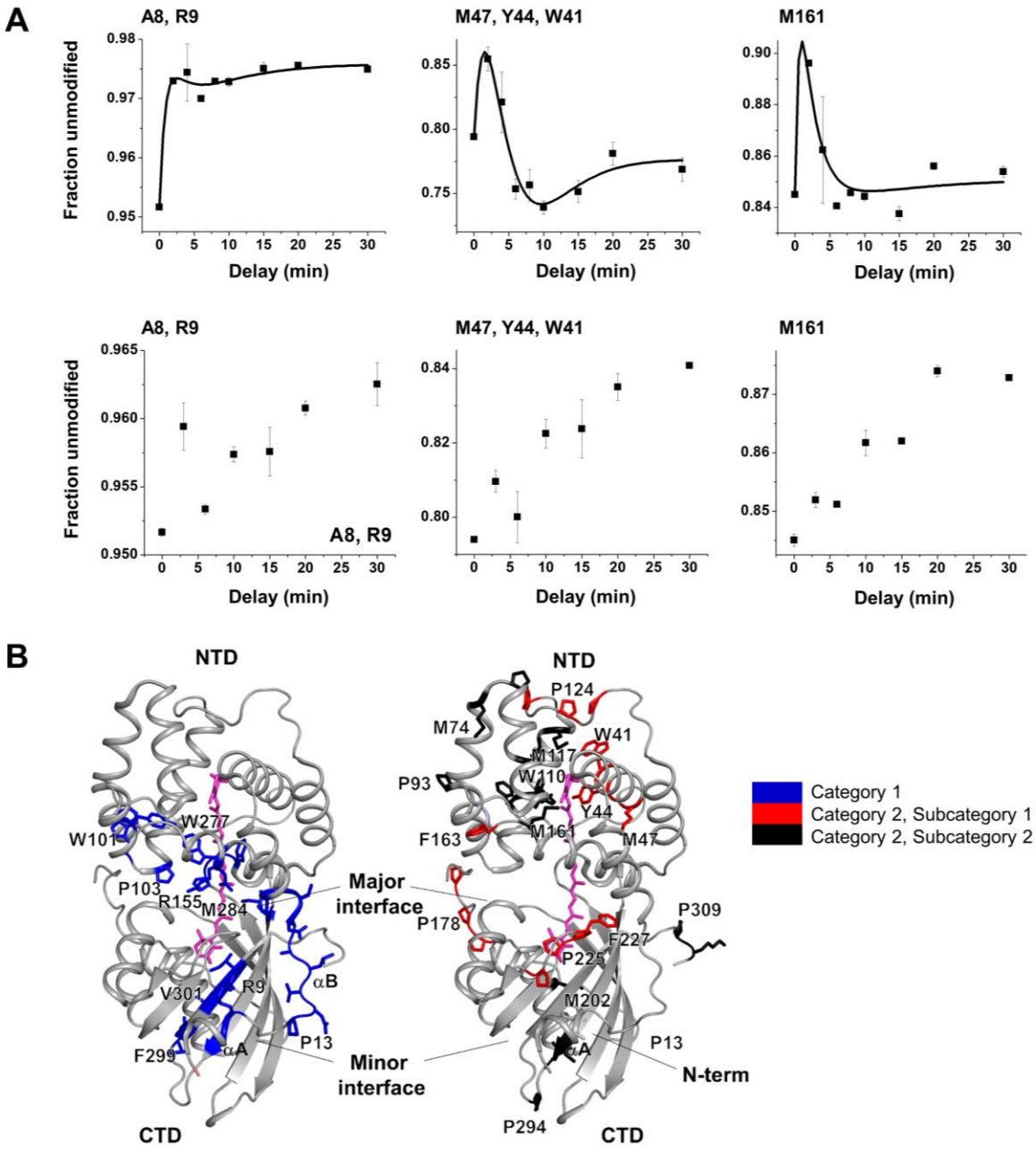

Figure 2. Time-evolution of local conformational changes in OCP^R relaxation
(A) Representative time-resolved SA progress curves for the relaxation process at 15°C**.** On the left is shown A8/R9 from the first category (fastest). The following two curves are in the slow category, representing two subsets within this category. Representative of the first subset is M47, Y44, and W41 in which there is a net SA change. Representative of the second subset is M161 in which there is no net accessibility change. The solid line represents three exponential fit of the time course of the unmodified fraction with the fitted lifetimes: τ_1, τ_2, and τ_3 for the kinetic phases

consisting of component 1, 2 and 3 respectively (Table S2). Error bars represent the standard deviation from three independent measurements. Below are the same experiments carried out at 4 °C, collecting accessibility changes from zero to thirty minutes in the OCP^R to OCP^O transition. (B) Residues in the two categories are mapped onto the OCP^O structure, PDB ID 3MG1. Carotenoid is in purple, residues in blue show a net SA decrease upon activation, and those in red and gray show a net increase and no change, respectively.

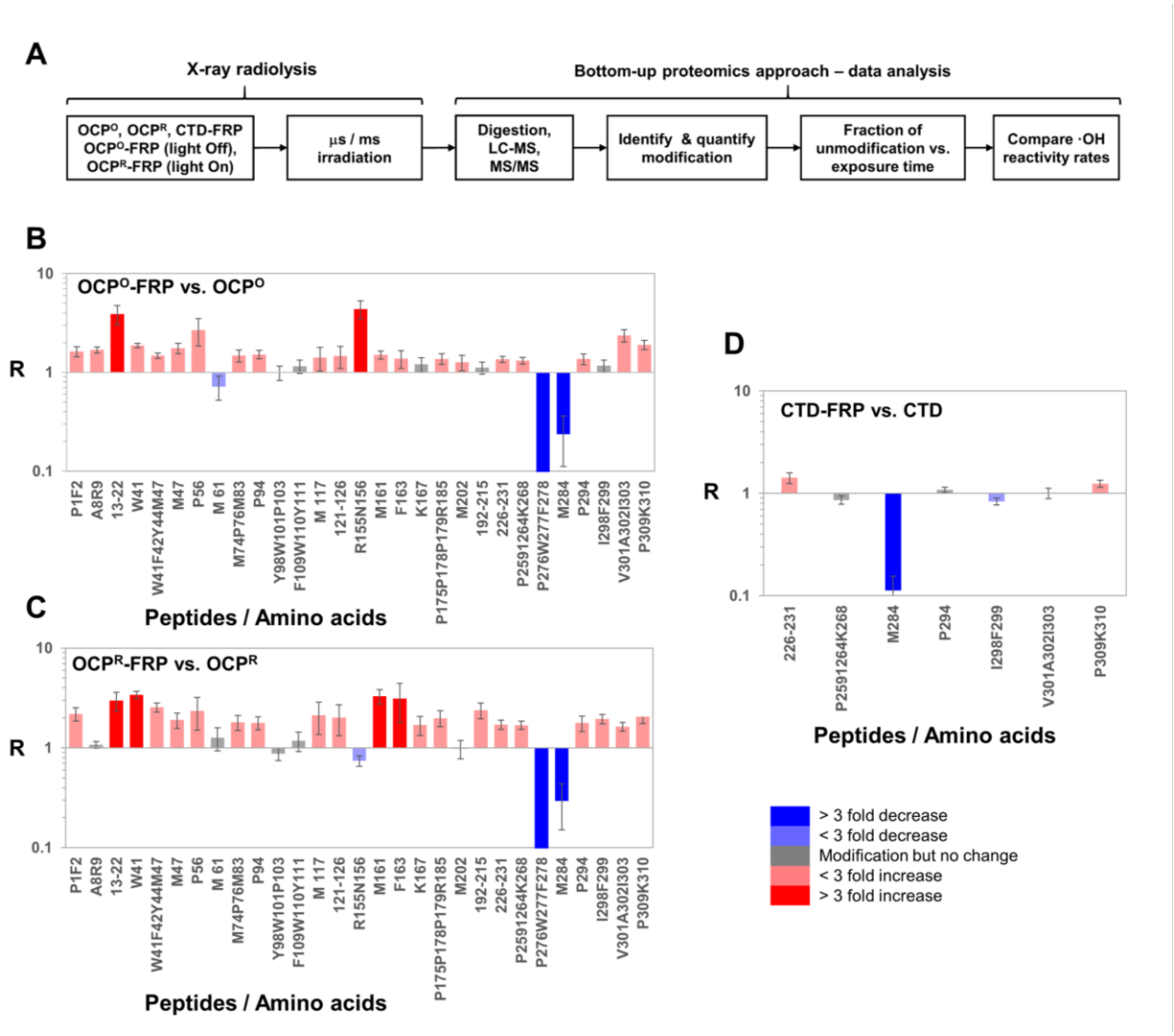

Figure 3. Footprint of the FRP on the OCP. (A) Experimental scheme. (B) The ratio (R) of rate constants between samples determines the relative SA differences arising from the FRP binding on OCP^O. Red indicates an increase in SA and blue indicates a decrease in SA of OCP residues when comparing the two states. (C) Relative SA difference arising from the FRP binding on OCP^R. (D) Relative SA differences arising from the FRP binding on CTD. The error bars represent the standard deviation from three independent measurements.

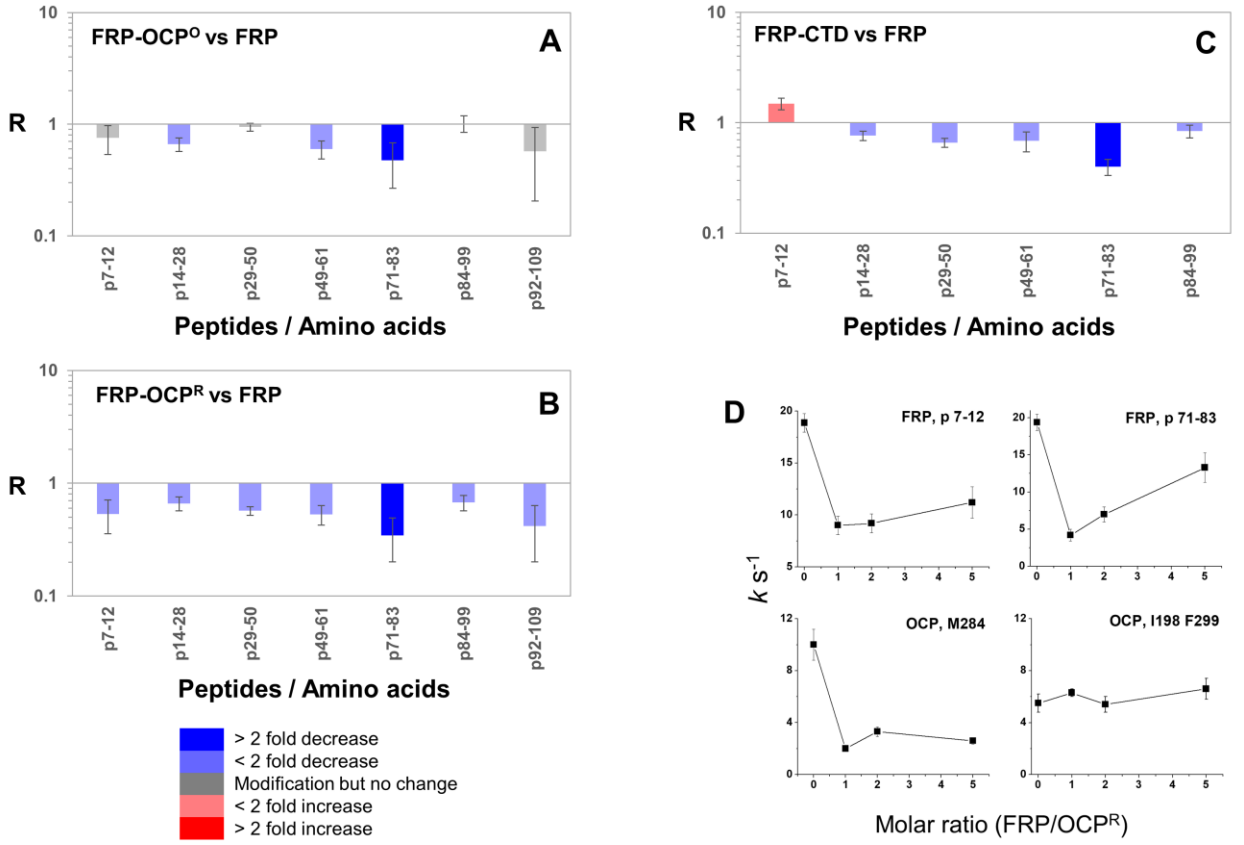

Figure 4. Footprint of the OCP on the FRP. The ratio (R) of rate constants between samples determines the relative SA differences arising from the FRP binding on OCP^O (A), OCP^R (B) and CTD (C). Red indicates an increase in SA and blue indicates a decrease in SA of FRP residues when comparing the two states. Error bars represent the standard deviation from three to six independent measurements. (D) Rate of reactivity of FRP and OCP peptides which are involved in binding interactions. The reactivity rate is obtained from the dose-response plots at various molar concentrations of FRP with respect to OCP^R.

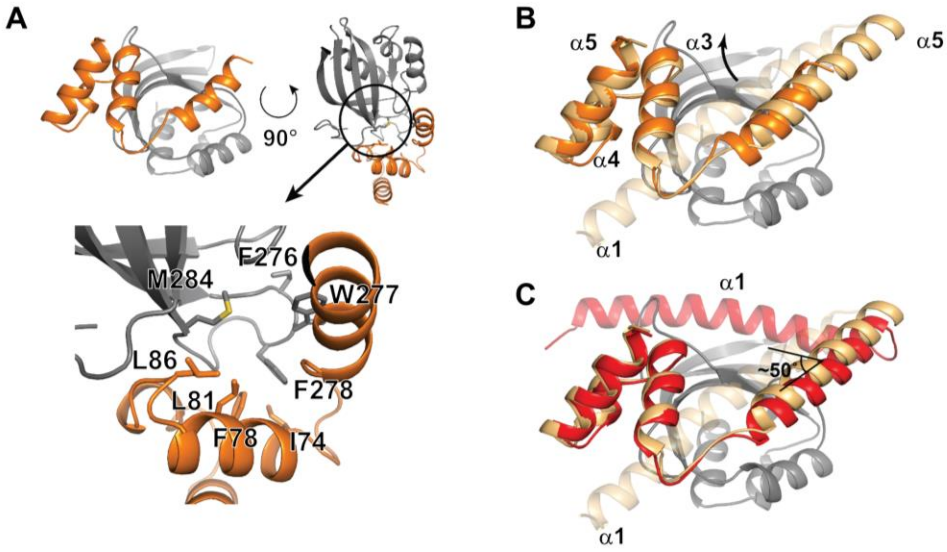

Figure. 5. Docked structure of FRP-CTD complex. (A) The major interface of the OCP-CTD (gray) and FRP monomer head domain (orange) form a complex. Zoomed region shows the highly hydrophobic binding interface and residues that undergo significant protection upon complex formation. (B) Superimposed view of the head domain complex with the structure of one chain of the FRP crystal structure dimer (light brown). The α1 helix of the crystal structure would clash with CTD if it were in the same conformation. (C) A ~ 50° rotation of the α1 leads to a favorable complex after docking simulation shown in red. The α1 helix of FRP is located where the N-terminal αA helix (OCP residues 13-22) is located in the OCP^O form.

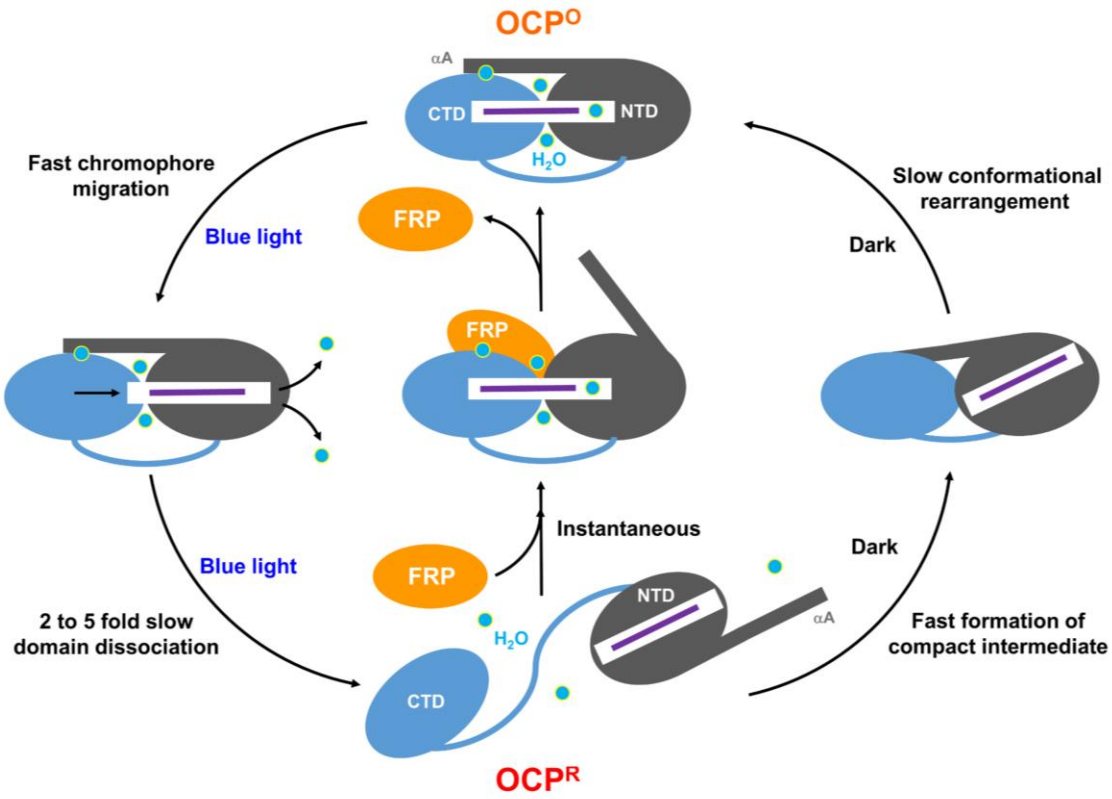

Figure 6. **Working model of photoprotection by the OCP.** Strong blue-green light induces OCP photoactivation, which is driven by fast carotenoid migration into the NTD. Slow domain dissociation leads to complete activation, where OCP^R exists as a fully dissociated form in which the two domains (NTD and CTD) are attached by a flexible linker. FRP can bind to the CTD of OCP^R and act as a scaffold for proper domain association and carotenoid configuration. Cyan circles are the position of bound and conserved waters, which are critical for the native OCP^O structure. Formation of a misfolded compact intermediate in the absence of FRP may slow the relaxation process. The FRP-induced transition from the red to the orange form occurs faster than is measurable.